

# Extreme vorticity events in turbulent Rayleigh-Bénard convection from stereoscopic PIV measurements and reservoir computing

Valentina Valori and Robert Kräuter  
*Institute of Thermodynamics and Fluid Mechanics,  
Technische Universität Ilmenau, D-98684 Ilmenau, Germany*

Jörg Schumacher  
*Institute of Thermodynamics and Fluid Mechanics,  
Technische Universität Ilmenau, D-98684 Ilmenau, Germany and  
Tandon School of Engineering, New York University, New York, NY 11201, USA*  
(Dated: May 16, 2022)

High-amplitude events of the out-of-plane vorticity component  $\omega_z$  are analyzed by stereoscopic particle image velocimetry in the bulk region of turbulent Rayleigh-Bénard convection in air. The Rayleigh numbers  $Ra$  vary from  $1.7 \times 10^4$  to  $5.1 \times 10^5$ . The experimental investigation is connected with a comprehensive statistical analysis of long-term time series of  $\omega_z$  and individual velocity derivatives  $\partial u_i / \partial x_j$ . A statistical convergence for derivative moments up to an order of 6 is demonstrated. Our results are found to agree well with existing high-resolution direct numerical simulation data in the same range of parameters, including the extreme vorticity events which appear in the far exponential tails of the corresponding probability density functions. The transition from a Gaussian to a non-Gaussian velocity derivative statistics in the bulk of a convection flow is confirmed experimentally. The experimental data are then also taken to train a recurrent neural network in the form of a reservoir computing model that is able to reproduce highly intermittent experimental time series of the vorticity and thus also to predict extreme out-of-plane vorticity events. In the prediction phase, the trained machine learning model is run with sparsely seeded, continually available measurement data. The dependence of the prediction quality on the sparsity of the partial observations is also documented. Our latter result paves the way to machine-learning-assisted experimental analyses of small-scale turbulence for which time series of missing velocity derivatives can be provided by generative algorithms.

## I. INTRODUCTION

Thermal convection is one the fundamental mechanisms by which the turbulent flows evolve. The temperature dependence of the fluid mass density and the resulting buoyancy forces drives fluid motion that in turn advects the temperature leading to a fully turbulent motion of the fluid [1–4]. The simplest configuration in this specific class of turbulent flows is Rayleigh-Bénard convection (RBC) – a fluid layer of height  $H$  between two parallel rigid plates heated uniformly from below and cooled uniformly from above, such that a constant temperature difference  $\Delta T = T_{\text{bot}} - T_{\text{top}} > 0$  is sustained across the layer. Experimentally, RBC can be realized in a horizontally extended closed cylindrical or cuboid cell with thermally insulated sidewalls. In the past two decades, a larger number of direct numerical simulations (DNS) of this configuration investigated various aspects of the large-scale structure formation, the longer-term dynamics and the dependencies on Rayleigh and Prandtl numbers,  $Ra$  and  $Pr$ , as well as on the aspect ratio  $\Gamma$  of the cells in detail [5–16]. The number of studies of RBC in air at a Prandtl number of  $Pr = 0.7$  by means of controlled laboratory experiments is much smaller, see e.g. refs. [17–21] for investigations in large-aspect-ratio setups. The three dimensionless control parameters of

RBC experiments are defined as follows,

$$Ra = \frac{g\alpha\Delta TH^3}{\nu\kappa}, \quad Pr = \frac{\nu}{\kappa}, \quad \Gamma = \frac{L}{H}. \quad (1)$$

Here,  $g$  is the acceleration due to gravity,  $\alpha$  the thermal expansion coefficient,  $\nu$  the kinematic viscosity,  $\kappa$  the thermal diffusivity, and  $L$  the horizontal length scale.

The dynamics and structure of the boundary layers of the velocity and temperature fields at the top and bottom of an RBC layer are essential for the amount of heat that can be carried from the bottom to the top in this configuration. In Valori and Schumacher [22], a dynamical connection between this dynamics and the small-scale intermittent motion in the bulk, in particular the formation of high-amplitude dissipation events, was established. Thermal and kinetic energy dissipation fields probe the magnitude of gradients of the temperature and velocity fields, respectively. Their amplitudes are known to be largest at the smallest scales [23–26]. In detail, it was shown in [22] how the formation of coherent plumes at the top and bottom and their subsequent collision or passing creates large temperature gradients in the bulk that cause the formation of localized shear layers [27]. These studies set one motivation for the present work.

In the present work, we want to study the velocity derivatives in the bulk of an RBC configuration experimentally by means of stereoscopic particle image velocimetry (SPIV) in the midplane of the horizontal cell. This allows us to obtain all three velocity components

$u_i(\mathbf{x}, t)$  in a horizontal measurement region  $A = 2.9H \times 2.2H$  and thus 7 out of the 9 components of the velocity gradient tensor field  $M_{ij}(\mathbf{x}, t) = \partial u_i / \partial x_j$ . These are the in-plane component  $\partial u_i / \partial x_j$  with  $i = 1, 2, 3$  and  $j = 1, 2$  and  $\partial u_3 / \partial x_3 = -(\partial u_1 / \partial x_1 + \partial u_2 / \partial x_2)$  via the incompressibility condition of the flow. Thus the out-of-plane component of the vorticity field  $\omega_3 = \partial u_2 / \partial x_1 - \partial u_1 / \partial x_2$  can be obtained and we have access to highly intermittent derivative fields in the bulk of the turbulent convection layer. We analyze the statistics of these 7 derivatives and probe their statistical convergence. Furthermore, the resulting probability density functions (PDFs) are found to agree to those of existing high-resolution DNS data from ref. [22] in a similar setup and the same parameter range.

The SPIV snapshot series contain a few extreme events in the form of intense vortex cores that sweep across the measurement plane  $A$ . In the second part of this work, we analyze their temporal growth and explore the capability of recurrent neural network (RNN) architectures to model time series of the out-of-plane vorticity component and thus to predict high-amplitude or extreme events [28]. More specifically, we therefore apply the reservoir computing model (RCM) [29, 30] which has been shown to successfully predict the time evolution of nonlinear dynamical systems and turbulent flows. See for example refs. [31–36] for applications to fluid dynamical problems. We show that an RCM with continually available sparse data is able to predict high-amplitude or extreme out-of-plane vorticity events which can be quantified by a squared vorticity integrated over  $A$  (see ref. [37] for a recent review).

The outline of the manuscript is as follows. In Sections IIA to IIC, details on the experiment and the machine learning algorithm are provided. Section IIIA discusses the results in respect to the vorticity and velocity derivative statistics. Furthermore, we investigate the dynamics of a particular high-vorticity event tracked in the experiment in Sec. IIIB. Section IIIC finally provides the results of the application of the RNN to predict the time evolution and the non-Gaussian PDFs with the extended tails. We conclude the work with a summary and an outlook in Section IV. For convenience, we will also switch from the notation  $u_1, u_2, u_3$ , and  $\omega_3$  for velocity and vorticity field components to  $u_x, u_y, u_z$ , and  $\omega_z$  in the following sections with coordinate  $z$  parallel to the inferred temperature gradient between top and bottom.

## II. METHODS

### A. Rayleigh-Bénard convection cell for pressurized air

The experimental set-up is a large aspect ratio Rayleigh-Bénard convection (RBC) cell, of size  $W \times W \times H$ , where the horizontal dimension  $W$  is ten times larger than the vertical distance between the two plates  $H$  that

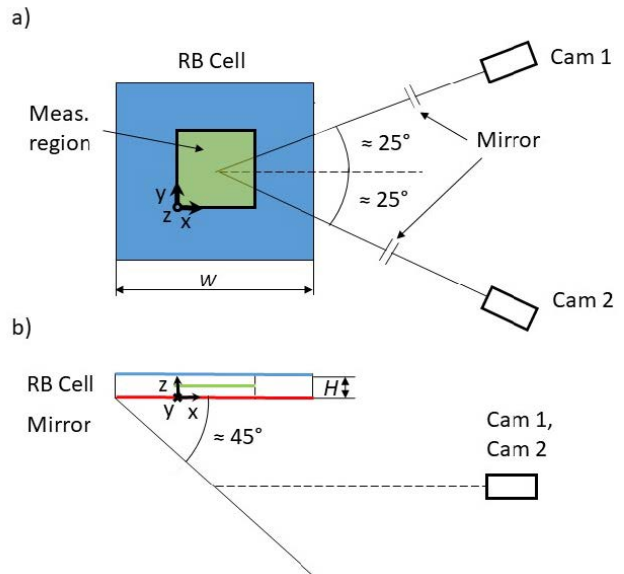


FIG. 1. Relative position of cameras, RBC cell and measurement section. a) top view, b) side view. The heated bottom plate of the RBC cell and the cooled top plate are indicated by a red and a blue lines, respectively. The measurement section  $A$  is represented in green in panels (a) and (b).

is 3 cm (see figure 1). The aspect ratio of the cell is therefore  $\Gamma = 10$ . The bottom plate of the cell is made of two glass plates coated on one side with a thin layer of Indium Tin Oxide. It has the important characteristic of being transparent and at the same time uniformly heatable by the Joule effect. The latter arises from the electrical current that goes through the oxide layer (for further details see [20]). Each plate has a measured light transmission coefficient of about 68% [20]. This coating was manufactured at the Fraunhofer Institute for Organic Electronics in Dresden (Germany). The top plate of the RBC cell is made of Aluminium with an internal cooling circuit where water flows at controlled temperature fed by a thermostat. The side walls are made of 4 mm thick polycarbonate that allows optical access for the laser light. The surface temperatures at both horizontal walls were measured by four thermoresistances PT100 (class B) for each plate, which were located 20 mm far from the side walls.

The RBC cell is inserted in the high-pressure facility, the Scaled Convective Airflow Laboratory Experiment (SCALEX). This facility consists of a high-pressure vessel with 35 observation windows, allowing for optical access from the outside. The pressure within the vessel can be regulated from 10-100 mbars to 8 bars in steps of about 100 mbars. The working pressure was measured with a Cerabar PMC131 sensor from Endress + Hauser AG. Further details on the device are for example summarized in ref. [20].

Ra	$T_{\text{top}} [^{\circ}\text{C}]$	$T_{\text{bot}} [^{\circ}\text{C}]$	$\Delta T$	p [bars]	$U_{\text{ff}}$ [mm/s]	$T_{\text{ff}}$ [s]
$1.7 \times 10^4$	22.3	28.9	6.6	1	80.7	0.4
$2.1 \times 10^4$	21.2	29.2	8	1	80.7	0.4
$1.1 \times 10^5$	21.2	28.5	7.3	2.47	85	0.35
$2.9 \times 10^5$	22.9	28.4	5.5	4.5	74.3	0.4
$5.1 \times 10^5$	20.1	29.9	9.8	4.5	98.8	0.3

TABLE I. Summary of the experimental conditions used in the convection measurements. The first column reports the Rayleigh numbers, the second and the third one the values of the top ( $T_{\text{top}}$ ) and bottom ( $T_{\text{bot}}$ ) temperatures, respectively, the fourth one the temperature difference between the bottom and the top walls ( $\Delta T$ ), the fifth one the working pressure. The sixth and the seventh columns are for the characteristic free-fall velocity and free-fall time of the flow, respectively.

### B. Particle image velocimetry measurements

Stereoscopic Particle Image Velocimetry experiments are performed in a horizontal layer at mid height between top and bottom plate of the cell. The position of the measurement plane is shown in green in figure 1. As already discussed, the measurement region covers a horizontal area of  $A \approx 2.9H \times 2.2H$ . In order to conduct stereo PIV measurements in a horizontal plane within the cell, two cameras are located below the cell and which take images through the transparent bottom plate. A mirror is placed in the optical path as represented in figure 1. A stereo angle of about  $50^{\circ}$  is used. The cameras are sCMOS from LaVision GmbH with digital resolution of  $2560 \times 2160$  pixels and a pixel pitch of  $6.5 \mu\text{m}$ . These cameras have particularly thin connector cables made of optical fibres that allow them to be placed inside the high-pressure vessel. These cables are inserted into feed through systems for high pressure from Spectite<sup>®</sup> that are built in a flange of the vessel. The images are recorded at a frame rate of 10 Hz with inter-frame time of 7 ms or 10 ms depending on the strength of the convective flow (or Rayleigh number Ra) studied. Each camera is equipped with a Zeiss Milvus 2/100M objective lens under the Scheimpflug condition. The focal length of the lenses is 100 mm and the aperture stop used is 5.6 and 8 for the camera in forward and backward scattering, respectively. Both cameras and lenses are placed inside the vessel at a working pressure of up to 4.5 bars. The field of view of the measurements is  $8.8 \text{ cm} \times 6.6 \text{ cm}$ . Therefore the image magnification factor is  $M \sim 0.2$ . The laser light sheet was created with a double pulse laser (Quantel Q-smart Twins 850) with a pulse energy of about 175 mJ for a 2 mm thick light sheet. A spherical and a cylindrical lens were used to generate the light sheet.

The depth of field of the measurements  $\delta_z$  is given by

$$\delta_z = 4\left(1 + \frac{1}{M}\right)^2 f_{\#}^2 \lambda, \quad (2)$$

Ra <sup>DNS</sup>	$\eta_K$ [mm]	Ra <sup>PIV</sup>	$\Delta x^{\text{PIV}}$ [mm]
$1.5 \times 10^4$	2.4	$1.7 \times 10^4$	4
$2 \times 10^4$	2.2	$2.1 \times 10^4$	4
$1 \times 10^5$	1.3	$1.1 \times 10^5$	4
$2 \times 10^5$	1.0	$2.9 \times 10^5$	4
$5 \times 10^5$	0.7	$5.1 \times 10^5$	3.5

TABLE II. Kolmogorov length scale from the direct numerical simulations (DNS) and spatial resolution of the PIV measurements computed without overlap for each of the five Rayleigh numbers studied. The simulations were conducted in a domain of  $\Gamma = 8$  with periodic boundary conditions at the side-walls at  $\text{Pr} = 1$  by a spectral element method, see ref. [22] for details.

where  $\lambda$  is the wavelength of the laser. Here,  $\lambda = 532 \text{ nm}$  for the green laser is used. For the camera in forward scattering with the smallest f-stop  $f_{\#}$ , the depth is  $\delta_z = 2.4 \text{ mm}$ , which is larger than the laser sheet thickness and therefore ensures good focusing conditions of the illuminated particles. The geometrical calibration is made on the measurement plane with the three-dimensional target 204-15 from LaVision, where the distance between two dots is 15 mm, the dot diameter and the level separation are both 3 mm. Additionally, a stereoscopic self-calibration is made and iteratively repeated with final mean residual displacement below 1 pixel. This final value cannot be further reduced because of the presence of optical distortions due to the temperature gradient [38, 39].

The seeding in the PIV measurements is established by droplets of di(2ethylhexyl)sebacate (DEHS) with average diameter of  $0.9 \mu\text{m}$  generated by a vaporizer from PIVTECH GmbH that is placed inside the pressure vessel. The characteristic velocity of the flow is estimated as the free fall velocity  $U_{\text{ff}} = \sqrt{\alpha g \Delta T H}$ , see also table I for the values of  $U_{\text{ff}}$  and  $\Delta T$ . The sedimentation velocity of the particles used as tracers is given by

$$u_S = \frac{d_p^2 (\rho_p - \rho_f)}{18 \mu g}, \quad (3)$$

where  $\rho_f$  and  $\mu = \rho_f \nu$  are, respectively, the density and the dynamic viscosity of the fluid at the mean temperature and pressure of the cell, and  $\rho_p$  is the mass density of the particles. The sedimentation velocity of the particles used is negligible as visible by the ratio  $u_S/U_{\text{ff}}$  that is about  $4 \cdot 10^{-6}$  or smaller for all flow conditions studied here. The particles faithfully follow the flow as indicated by the values of the Stokes number  $\text{St}$  defined in eq. (4), which expresses the ratio between the characteristic time of a particle of diameter  $d_p$  and mass density  $\rho_p$  suspended in the flow and the characteristic time of the flow. Values of the Stokes number in the present study are always smaller than 0.01, as requested for good tracers particles [40, 41].

$$\text{St} = \frac{d_p \rho_p U_{\text{ff}}}{18\mu g} \quad (4)$$

The PIV images are acquired and processed with the software DaVis 10 from LaVision. The only preprocessing that is applied to the raw images is a time-averaged image subtraction in order to reduce the noise. A two-passes cross-correlation algorithm with decreasing interrogation window size is used. The size of the final pass is  $128 \times 128$  pixels for all measurements except for the largest Rayleigh number where the size is  $96 \times 96$ , which leads to a spatial resolution of about 4 mm and 3.5 mm, respectively (see table II). Here, we also list the Kolmogorov length  $\eta_K$  of the DNS (at the comparable Rayleigh numbers) which are given in dimensionless units by

$$\eta_K = \left( \frac{\text{Pr}}{\text{Ra}} \right)^{3/8} \langle \epsilon \rangle_{V,t}^{-1/4}, \quad (5)$$

where  $\langle \epsilon \rangle_{V,t}$  is the combined volume-time average of the kinetic energy dissipation rate field [24]. This value is multiplied by the actual cell height  $H$  to get a length in physical units as shown in the table.

The values of Rayleigh numbers of the experiments range from  $\text{Ra} = 1.7 \times 10^4$  to  $\text{Ra} = 5.1 \times 10^5$  and are listed in table I. The working fluid is air with  $\text{Pr} = 0.7$  for all cases. Rayleigh numbers  $\text{Ra} \geq 1.1 \times 10^5$  are obtained by putting the vessel under pressure. In table I the corresponding values of the working pressure of each experiment are shown together with the values of the temperatures at the bottom ( $T_{\text{bot}}$ ) and top ( $T_{\text{top}}$ ) walls of the cell in addition to the resulting difference  $\Delta T$ . The last two columns of the table indicate the characteristic free-fall velocity  $U_{\text{ff}}$  and resulting free-fall time  $T_{\text{ff}} = H/U_{\text{ff}}$  of the flow. Values of the fluid properties are taken from the NIST RefProp database version 9.1 [42].

### C. Reservoir computing model

In the following, we briefly review the reservoir computing model (RCM) [29]. The reservoir is a random, recurrently and sparsely connected network. The model consists of the input layer, the reservoir, and the output layer as shown in figure 2(a). The input layer takes the training data in the form of discrete time series  $\mathbf{\Omega}(t) = (\omega_z^{(1)}(t), \dots, \omega_z^{(N_{\text{PIV}})}(t))$  with  $N_{\text{PIV}}$  the number grid points of the PIV measurement region  $A$ . Vorticity data are converted at each instant into a reservoir state vector  $\mathbf{r}(t) \in \mathbb{R}^N$  with a number of reservoir nodes  $N \gg N_{\text{PIV}}$ . This is done by a random weight matrix  $W^{(\text{in})} \in \mathbb{R}^{N \times N_{\text{PIV}}}$  which is determined at the beginning of the training and left unchanged,

$$\mathbf{r}(t) = W^{(\text{in})} \mathbf{\Omega}(t). \quad (6)$$

The reservoir is described by a symmetric adjacency matrix  $W^r \in \mathbb{R}^{N \times N}$ , also determined initially and left unchanged. Typically, an ensemble of different realizations of the reservoir matrix is considered in the training process. Two important parameters of  $W^r$  are the reservoir density  $D$  of active nodes and the spectral radius  $\rho(W^r)$ , which is set by the largest absolute value of the eigenvalues. The reservoir nodes are updated by a simple nonlinear dynamical system evolves which comprises the short-term memory of the network,

$$\mathbf{r}(t + \Delta t) = (1 - \alpha)\mathbf{r}(t) + \alpha \tanh \left[ W^r \mathbf{r}(t) + W^{(\text{in})} \mathbf{\Omega}(t) \right], \quad (7)$$

where nonlinearity enters in the form of an activation function by a hyperbolic tangent. The leakage rate is  $0 < \alpha < 1$  and the spectral radius of the reservoir is typically taken  $\rho(W^r) \lesssim 1$ . The final of the three building blocks of the RCM is the random output weight matrix  $W^{(\text{out})} \in \mathbb{R}^{N_{\text{PIV}} \times N}$  which maps the updated reservoir vector back to the vorticity field,

$$\hat{\mathbf{\Omega}}(t + \Delta t) = W^{(\text{out})} \mathbf{r}(t + \Delta t). \quad (8)$$

The iteration of (7) is repeated for the all snapshots of the PIV training data and the sequence of corresponding reservoir states is saved. In contrast to most other neural networks, the training of the RCM is performed with respect to the output layer only. The optimized output weight matrix,  $W^{(\text{out})*}$ , is obtained by a minimization of a regularized quadratic cost function  $C$ . The regularization term is added to  $C$  to tackle the over-fitting problem [28]. This cost function is given by

$$C \left[ W^{(\text{out})} \right] = \sum_{k=1}^{N_{\text{train}}} \left| W^{(\text{out})} \mathbf{r}(k\Delta t) - \mathbf{\Omega}(k\Delta t) \right|^2 + \gamma \text{Tr} \left( W^{(\text{out})} W^{T(\text{out})} \right). \quad (9)$$

To summarize, the hyperparameters of the RCM training process are the number of nodes  $N$ , the reservoir density  $D$ , the spectral radius  $\rho(W^r)$ , the leakage rate  $\alpha$ , and the ridge regression parameter  $\gamma > 0$  of the regularization term of the cost function  $C$ . These parameters span a 5-dimensional space and have to be tuned, e.g., by a grid search, such that optimal output matrix  $W^{(\text{out})*}$  results and a mean square error between prediction and test data becomes minimal.

In the subsequent prediction mode, the RCM predicts the vertical vorticity component field in the measurement region that can be compared with original unseen test data. The reservoir dynamics in prediction mode is given by

$$\mathbf{r}(t + \Delta t) = (1 - \alpha)\mathbf{r}(t) + \alpha \tanh \left[ W^r \mathbf{r}(t) + W^{(\text{in})} W^{(\text{out})*} \mathbf{r}(t) \right]. \quad (10)$$

More details can be found in refs. [30, 35]. The dynamics of eq. (10) is used to generate synthetic time series of the

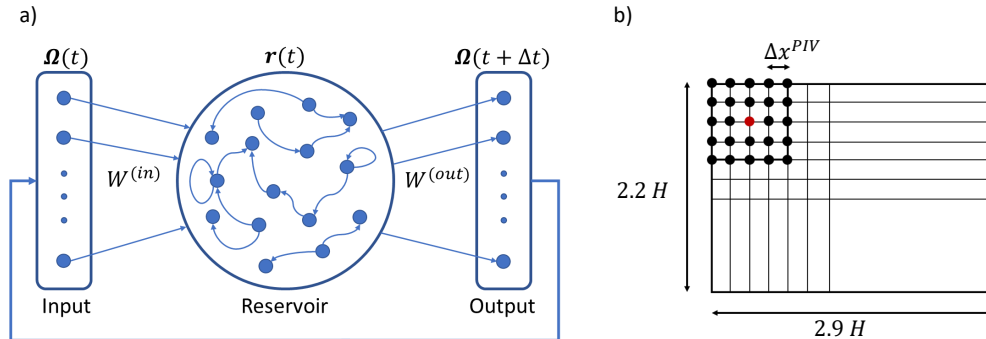


FIG. 2. Sketch of the reservoir computing model (RCM) and arrangement of continually available data during the prediction phase of the machine learning algorithm. (a) The three building blocks of the RCM are the input layer, the reservoir (a random network of neurons), and the output layer. (b) Sketch of a part of the data grid  $A$  obtained in the stereoscopic particle image velocimetry (PIV) measurement. This figure illustrates the  $5 \times 5$  scenario: one data point with continually available experimental vorticity data (in red) is surrounded by 24 grid points for which the trained RCM predicts the time evolution of the vorticity component autonomously. The whole measurement area  $A$  is covered sparsely with continually available measurements in this way. The uniform PIV resolution is also indicated.

intermittent vorticity component at the grid points of the measurement region  $A$ .

### III. RESULTS

#### A. Velocity derivative statistics

The long total measurement acquisition time of 2500  $T_{ff}$  allows a good convergence of the statistics as displayed in figure 3. In these plots, we report results of the out-of-plane vorticity and selected individual velocity derivative components, all normalized by their corresponding root-mean-square (rms) values. We therefore define

$$\chi := \frac{\omega_z}{\sqrt{\langle \omega_z^2 \rangle_{A,t}}} \quad \text{or} \quad \chi := \frac{\partial u_i / \partial x_j}{\sqrt{\langle (\partial u_i / \partial x_j)^2 \rangle_{A,t}}}, \quad (11)$$

with  $i, j = 1, 2, 3$ . The denominators in both equations are the root-mean-square (rms) values of the corresponding quantities. The statistical convergence of the  $n$ -th order normalized moment follows from plots of  $\chi^n p(\chi)$  versus  $\chi$ . The area below these curves corresponds then to the  $n$ -th order moment  $M_n$  which is given by

$$M_n(\chi) := \int_{-\infty}^{\infty} \chi^n p(\chi) d\chi. \quad (12)$$

These moments can be evaluated in a discretized approximation of this integral. The statistical convergence of moments  $M_2$ ,  $M_4$ , and  $M_6$  is shown in figure 3 for the two largest experiment Rayleigh numbers  $Ra = 2.9 \times 10^5$  and  $Ra = 5.1 \times 10^5$ . A converged velocity derivative statistics implies that the tails for the largest  $\chi$ -values tend to decay to zero which seems to be case for the shown components. Note that  $y$ -axes are displayed in logarithmic units in the figure. We have also verified that the two velocity gradient tensor components which are not shown

in the figure satisfy the statistical convergence criteria as well. It can be confirmed that the PIV measurements obtain sufficiently well-resolved velocity gradients in the range of accessible Rayleigh numbers.

Figure 4 reports a direct comparison between the PDFs of 5 components of the velocity gradient tensor  $A_{ij}$  and the out-of-plane vorticity component  $\omega_z$  from the SPIV measurements and the DNS data from [22]. One can see that the experimental results are in very good agreement with the simulation data all the way to the far tails. Again, the PDFs of the 2 missing components,  $\partial u_z / \partial x$  and  $\partial u_z / \partial y$ , are qualitatively and quantitatively similar to the shown data.

The PDFs of the out-of-plane vorticity of the SPIV of all series as displayed in table II are shown in figure 5, respectively. One can observe that the tails of the PDFs become wider as the Rayleigh number grows, which is an indication of a transition from Gaussian to non-Gaussian intermittent velocity derivative statistics as discussed for RBC in refs. [22, 43, 44]. We can thus conclude that this transition is also detectable in the bulk of controlled laboratory experiments at moderate Rayleigh numbers. This allows to run long-term measurements of velocity derivative statistics which is challenging in simulations where the numerical effort grows with  $\Gamma^2$ .

#### B. Extreme event of out-of-plane vorticity

An example of an extreme event of  $\omega_z$  from PIV measurements at Rayleigh number  $Ra = 5.1 \times 10^5$  is shown in figure 6. We count an extreme event whenever the vorticity magnitude exceeds  $10\omega_{z,rms}$ . In the time interval at the highest Rayleigh number, we were able to record two of these events. It can be expected that their frequency and excess magnitude increase when the Rayleigh number grows. We have to leave this point for future work.

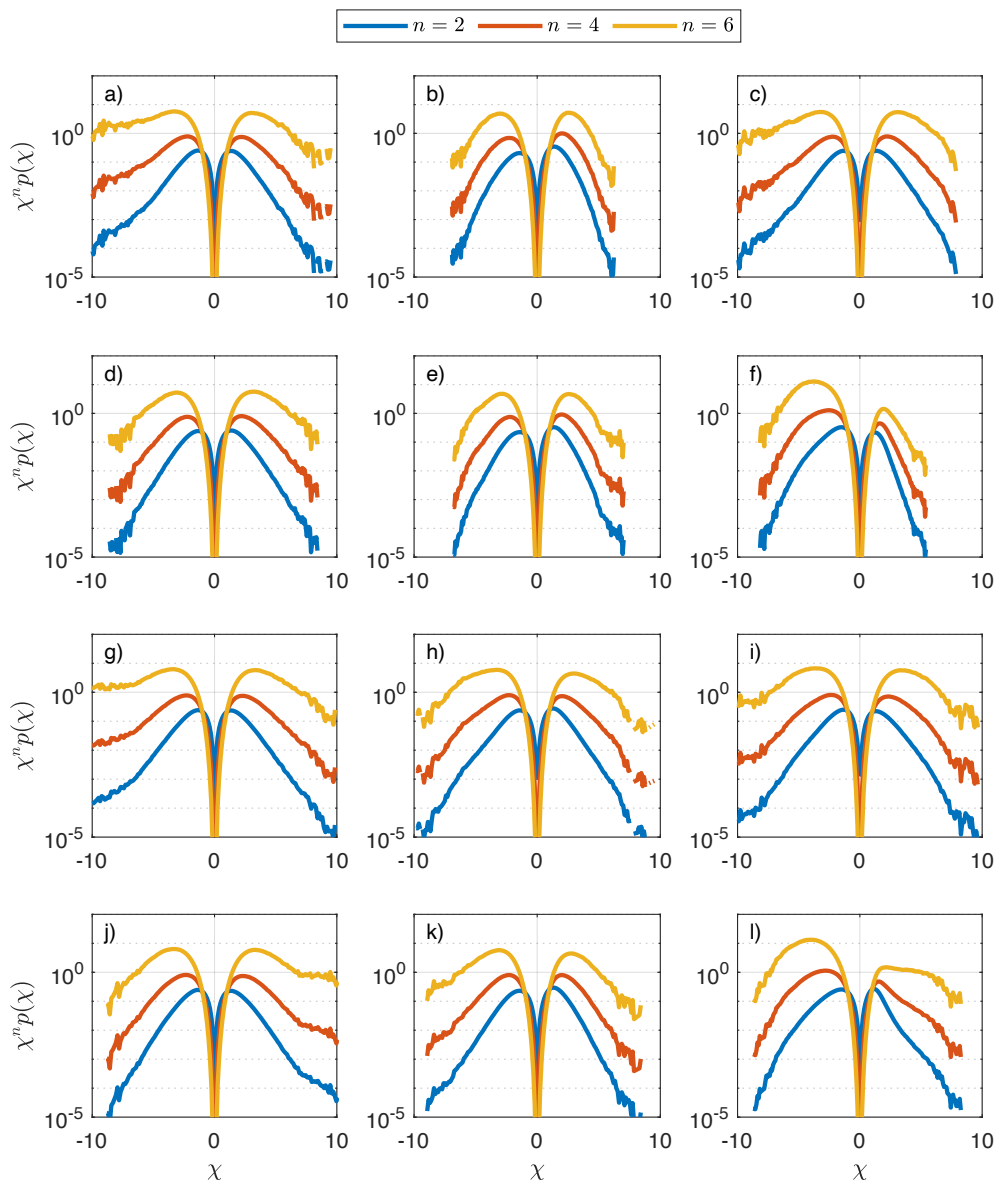


FIG. 3. Statistical convergence of the higher-order velocity derivative statistics in the experiments. The vorticity component  $\omega_z$  (a,g) and the derivatives  $\partial u_x/\partial x$  (b,h),  $\partial u_y/\partial x$  (c,i),  $\partial u_x/\partial y$  (d,j),  $\partial u_y/\partial y$  (e,k), as well as  $\partial u_z/\partial z$  (f,l) are shown. All derivatives are normalized by their corresponding root mean square values. The moment order  $n$  is indicated in the legend above the panels. Panels (a–f) are for  $Ra = 2.9 \times 10^5$ , panels (g–l) for  $Ra = 5.1 \times 10^5$ .

Panel (a) of the figure shows a prominent vortex core on the right hand side of  $A$ . This vortex is the results of a horizontal shear in combination with an upward motion through the observation plane. From the corresponding velocity field, whose components are represented in panels (b–d) of this figure, one can suspect that a plume collision is responsible for the generation of the extreme vorticity event, as it was observed so far only in DNS data records [22].

Lu and Doering [45] showed that the temporal growth

of the enstrophy, which is given by

$$\bar{E}(t) = \int_V \omega_i^2 dV \quad \text{with} \quad \omega_i(\mathbf{x}, t) = \varepsilon_{ijk} \frac{\partial u_k(\mathbf{x}, t)}{\partial x_j}, \quad (13)$$

in homogeneous isotropic turbulence in a triply periodic box of volume  $V$ , is rigorously bounded by

$$\frac{d\bar{E}(t)}{dt} \leq \frac{27c^3}{16\nu} \bar{E}(t)^3, \quad (14)$$

with  $c = \sqrt{2/\pi}$ . It was found that axially symmetric, colliding vortex rings maximize the enstrophy growth and

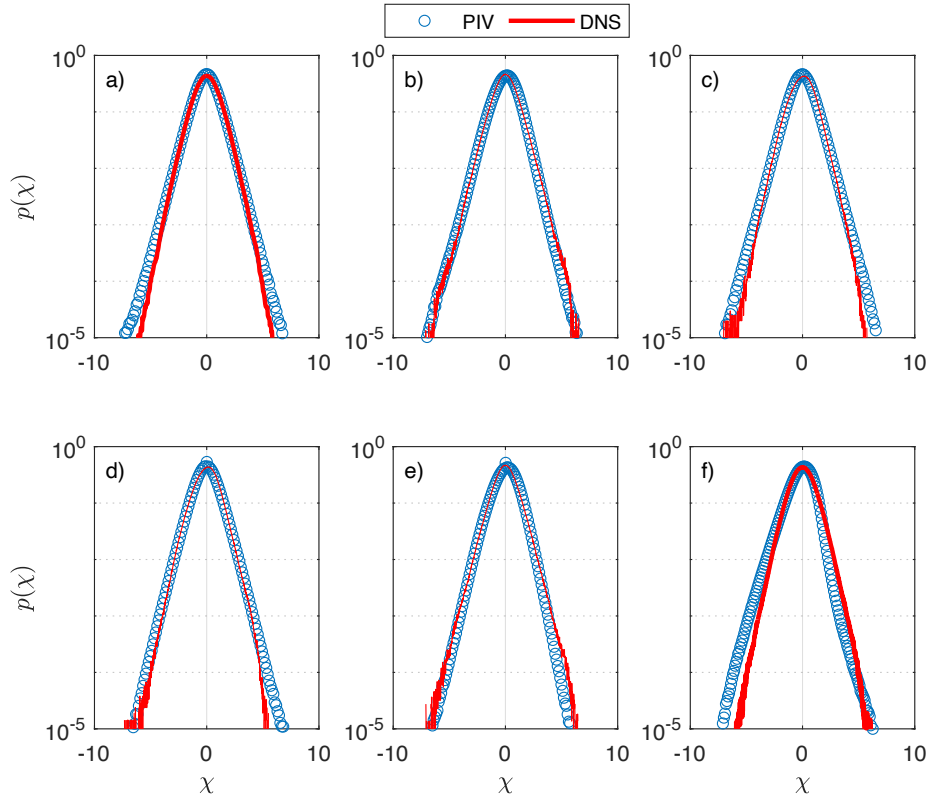


FIG. 4. Comparison of the probability density function of out-of-plane vorticity  $\omega_z$  (a) and the five partial derivatives, which are  $\partial u_x/\partial x$  in (b),  $\partial u_y/\partial x$  in (c),  $\partial u_x/\partial y$  in (d),  $\partial u_y/\partial y$  in (e), and  $\partial u_z/\partial z$  in panel (f). The PIV experiments are at  $Ra = 5.1 \times 10^5$ , the DNS at  $Ra = 5 \times 10^5$ . All quantities are normalized by their corresponding root-mean-square values.

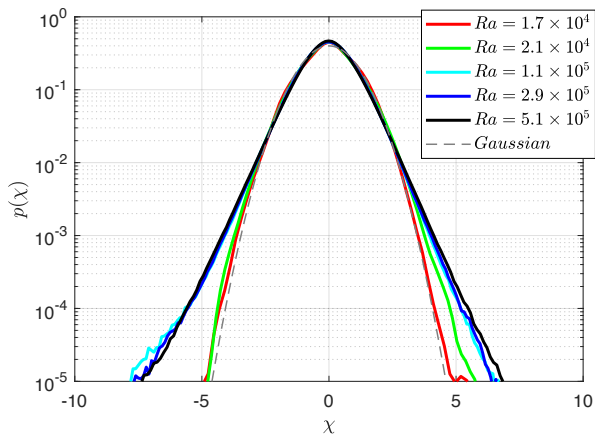


FIG. 5. Probability density functions (PDFs) of the out-of-plane vorticity field component obtained from different stereoscopic particle image velocimetry measurements for the Rayleigh numbers which are indicated in the legend. The gray dashed line displays the Gaussian case for reference.

that interacting Burgers vortices cause a growth  $d\bar{E}/dt \sim \bar{E}(t)^{7/4}$ . Even though we cannot expect that the same bound holds for a turbulent convection flow, we can probe the growth of the out-of-plane squared vorticity in the

measurement region  $A$ .

In figure 7, we therefore plot the temporal growth of the vorticity component,  $d\omega_z^2/dt$ , versus the squared vorticity,  $\omega_z^2$ , as a scatter plot for all grid points which are centered around  $\mathbf{x}_* \in A$ , the point where  $\omega_z^2$  yields an extreme event at time  $t = t_*$ . In both panels the time series (which extend over  $10^4$  data points) are plotted for  $5 \times 5$  grid points. The data right before  $t = t_*$  are replotted in blue in both panels. In addition, the growth laws with the exponents 3 and 7/4 are also indicated by solid lines. It is seen that for the highest-amplitude extreme event the growth to the maximum is close to the 7/4-scaling which suggests that a vortex stretching process generates this event. Further details cannot be provided on the basis of the measurements due to the missing vorticity derivatives.

### C. Reservoir computing model for dynamical evolution of vorticity

Finally, we apply a reservoir computing model (RCM) to predict the dynamical evolution of time series of  $\omega_z$  which are taken at specific points in the measurement region  $A$ . The corresponding procedure is visualized in figure 2(b) and follows the one of Lu et al. [31] taken to

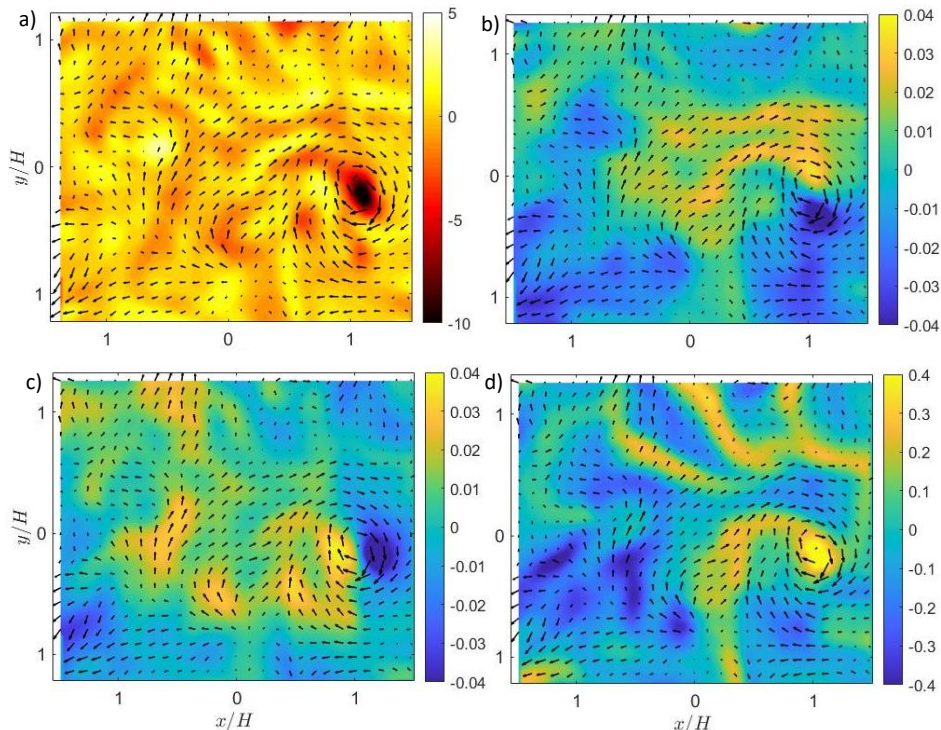


FIG. 6. Visualisation of an extreme event of  $\omega_z$  from the SPIV measurements at  $Ra = 5.1 \times 10^5$ . Filled contours of  $\omega_z$  in (a),  $u_x$  in (b),  $u_y$  in (c), and  $u_z$  in (d) are shown. Color bars of the vorticity and velocity components are given in units of  $t_{ff}$  and  $U_{ff}$ , respectively. Arrows show the same in-plane velocity vector field in all four panels.

predict the dynamics of the one-dimensional Kuramoto-Sivashinsky equation: for the prediction phase, we provide time series of the measurements sampled on a very coarse uniform grid that covers the measurement region  $A$ . This implies that the prediction in the present case is obtained with the help of continually available, partial observations. The RCM is then trained to generate vorticity time series at the remaining and surrounding grid points of the measurement region  $A$ . The procedure allows us to reconstruct the dynamics of the vorticity component in  $A$ .

In table III, we summarize the optimal hyperparameters of the RCM that are chosen after the training procedure for the time series prediction. All time series consist of  $10^4$  PIV snapshots. The first  $N_T = 5000$  snapshots were used to train the RCM model, the remaining  $N_P = 5000$  data snapshots are test data. Furthermore, we list the mean squared errors (MSE) in the table which follow for the training and prediction phases. These errors are given by

$$\text{MSE}_{T,P} = \frac{1}{N_{T,P}} \sum_{n=1}^{N_{T,P}} \frac{1}{N_{PIV}} \sum_{k=1}^{N_{PIV}} (\Omega_k(n) - \hat{\Omega}_k(n))^2, \quad (15)$$

where  $\Omega(n)$  is the ground truth and  $\hat{\Omega}(n)$  the RCM prediction.

Three different scenarios, namely learning the vorticity time series on  $3 \times 3$ ,  $5 \times 5$ , and  $7 \times 7$  grid points around

	$Ra = 1.7 \times 10^4$			$Ra = 2.9 \times 10^5$		
	$3 \times 3$	$5 \times 5$	$7 \times 7$	$3 \times 3$	$5 \times 5$	$7 \times 7$
$N$	2936	2526	2816	1522	2109	2469
$\alpha$	0.79	0.12	0.19	0.45	0.58	0.38
$\rho(W^r)$	0.99	0.99	0.96	0.99	0.96	0.98
$\gamma$	0.27	0.13	0.09	0.01	0.04	0.12
$D$	0.2	0.2	0.2	0.2	0.2	0.2
$\text{MSE}_T$	0.028	0.027	0.048	0.075	0.204	0.29
$\text{MSE}_P$	0.040	0.22	0.32	0.25	0.49	0.79

TABLE III. Summary of the optimal hyperparameters. Here, each run was trained individually. Furthermore, the mean squared error (MSE) of the training (T) and prediction phases (P) is given. The optimal parameters were chosen for  $N \in [1000, 3000]$ ,  $\rho(W_r) \in [0.9, 1]$ ,  $\gamma \in [0.01, 1]$ , and  $\alpha \in [0.1, 1]$ . For each of 10 different random configurations of the reservoir matrix  $W^r$  100 different random combinations of the hyperparameters within the given intervals were taken.

continually provided data points have been investigated. We have conducted this analysis for the smallest and one of the largest Rayleigh numbers of our data record,  $Ra = 1.7 \times 10^4$  and  $2.9 \times 10^5$ . The results are summarized correspondingly in figures 8 and 9. Panels (a) and (b) in each of both figures display the prediction of an example of a time series taken at a specific position in  $A$ .

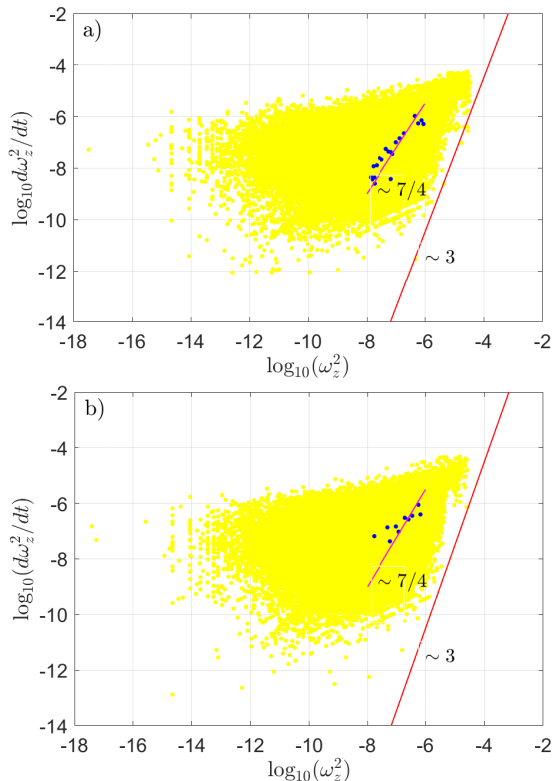


FIG. 7. Scatter plots of the time series, taken at the 25 grid points around extreme event position  $\mathbf{x}_*$  for  $Ra = 5.1 \times 10^5$ . Panels (a) and (b) stand for the two events at  $t = 853.25t_{ff}$  and  $t = 599t_{ff}$ , respectively, for which  $|\omega_z| \geq 10\omega_{z,rms}$ . The squared out-of-plane vorticity growth is plotted versus squared out-of-plane vorticity. The final data points with  $t < t_*$  are replotted in blue. Also indicated are the scaling exponents that follow from [45].

We see that in both cases the time dependence is approximated fairly well by the reservoir computing model. Both figures are obtained for a  $5 \times 5$  reconstruction scenario. Panel (b) magnifies the initial time steps  $n$  of the prediction phase. Panels (c) and (d) of both figures display the PDFs that result for the normalized vorticity component from the RCM in comparison to the experimental test data. While the velocity derivative statistics for the smallest Rayleigh number is still very close to a Gaussian distribution, it has crossed over to the non-Gaussian intermittent regime for the higher Rayleigh number. This becomes visible by the extended tails that are also reproduced well by our machine learning algorithm. The PDFs in both panels are shown for two scenarios,  $3 \times 3$  and  $7 \times 7$ , in each case. Note that the latter scenario implies that less input is provided for the machine learning algorithm during the prediction phase. Only each 48th grid point contains a partial observation. We can see again that the statistics in both cases is in fair agreement with the experimental results. The RCM with continually available sparse data is thus able to predict the statistical

properties of a highly intermittent out-of-plane vorticity component.

In figure 10, we demonstrate the capability of the trained recurrent neural network to predict an extreme vorticity event. A typical event, which is detected at a time  $t = t_*$  (that translates into snapshot number  $n = n_*$ ) is shown here. We therefore compare a sequence of PIV snapshots with the corresponding model predictions. The RCM results have been composed of  $3 \times 3$  predictions. The panels have been subsequently smoothed by a  $6 \times 6$  procedure averaging. It can be seen that the figures at the corresponding times agree well with each other. We can thus conclude from this visual inspection that extreme or high-amplitude vorticity events are predictable by the specific recurrent machine learning algorithm. We also note here that for a prediction without partial observations, i.e., for a fully autonomous RCM prediction, the time series at the grid points of the measurement section  $A$  start to deviate after a few time steps  $n$  for the highest Rayleigh numbers of our data record.

In figure 11, the squared out-of-plane vorticity or out-of-plane enstrophy  $E(t)$  is integrated over the observation plane  $A$ . The quantity is given by

$$E(t) := \int_A \frac{\omega_z^2(t)}{2} dA, \quad (16)$$

and displayed for two Rayleigh numbers. The snapshot number of the global vorticity component maximum is denoted as  $n_*$ . The quantitative comparison of the 3 predictions with the experimental test data demonstrates that all 3 scenarios follow the ground truth data fairly well. As expected, the deviations increase with increasing spatial sparsity of the available partial observations.

#### IV. SUMMARY AND OUTLOOK

Our present work was motivated by two major scientific objectives: (1) the detailed analysis of the intermittent statistics of velocity derivatives in the bulk of a turbulent Rayleigh-Bénard convection flow in air by means of stereoscopic particle image velocimetry measurement including the monitoring of high-amplitude events of the out-of-plane vorticity component and (2) the machine-learning-assisted reconstruction of the dynamical evolution and statistics of the small-scale velocity derivatives including the prediction of extreme or high-amplitude events. Therefore, the moderate Rayleigh numbers were varied over an order of magnitude, in a range for which the statistics of the spatial velocity derivatives (and thus of the vorticity components) goes over from Gaussian to non-Gaussian, as discussed in our recent direct numerical simulations [22]. This transition in the derivative statistics was detected by both, the experiments and the subsequent machine learning algorithm which is based on a recurrent neural network.

As in most laboratory experiments and in contrast to direct numerical simulations the three velocity compo-

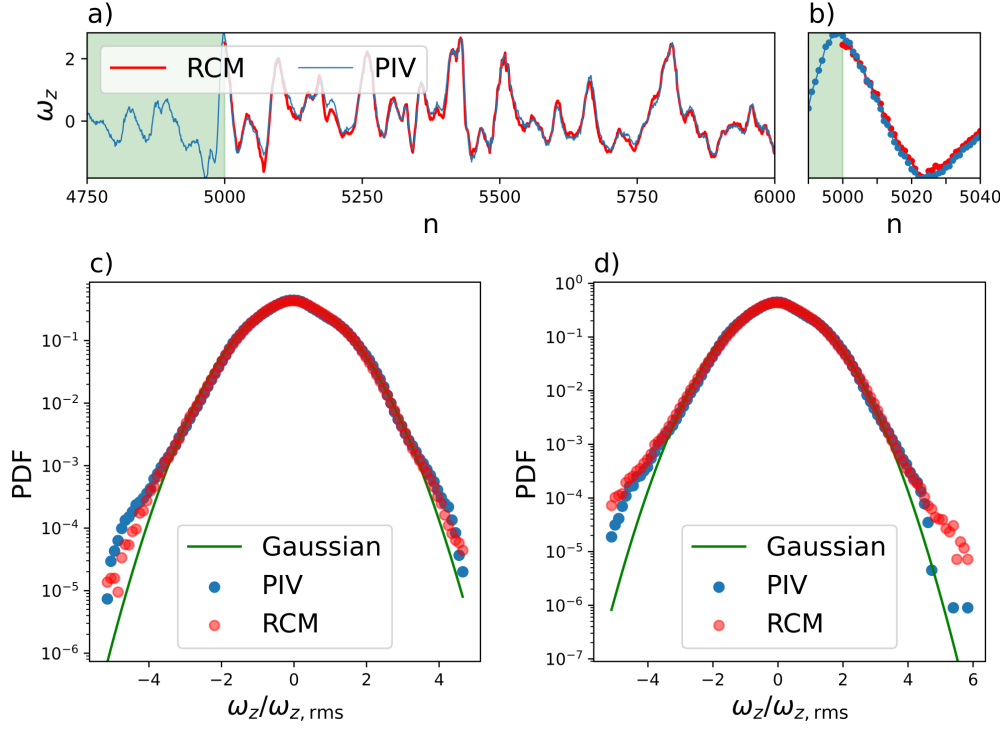


FIG. 8. Prediction of temporal evolution and statistics of the out-of-plane vorticity component  $\omega_z$  by reservoir computing models. The Rayleigh number is  $Ra = 1.7 \times 10^4$ . (a) Time series prediction example at one grid point in  $A$ . Integer  $n$  corresponds to time  $n\Delta t$  with  $\Delta t = 0.25t_{ff}$ . (b) Zoom into the first steps of the prediction phase. Panel (c) shows the probability density function obtained from a prediction of correspondingly 8 grid points around each continually available data point (scenario  $3 \times 3$ ) and panel (d) from 48 grid points (scenario  $7 \times 7$ ).

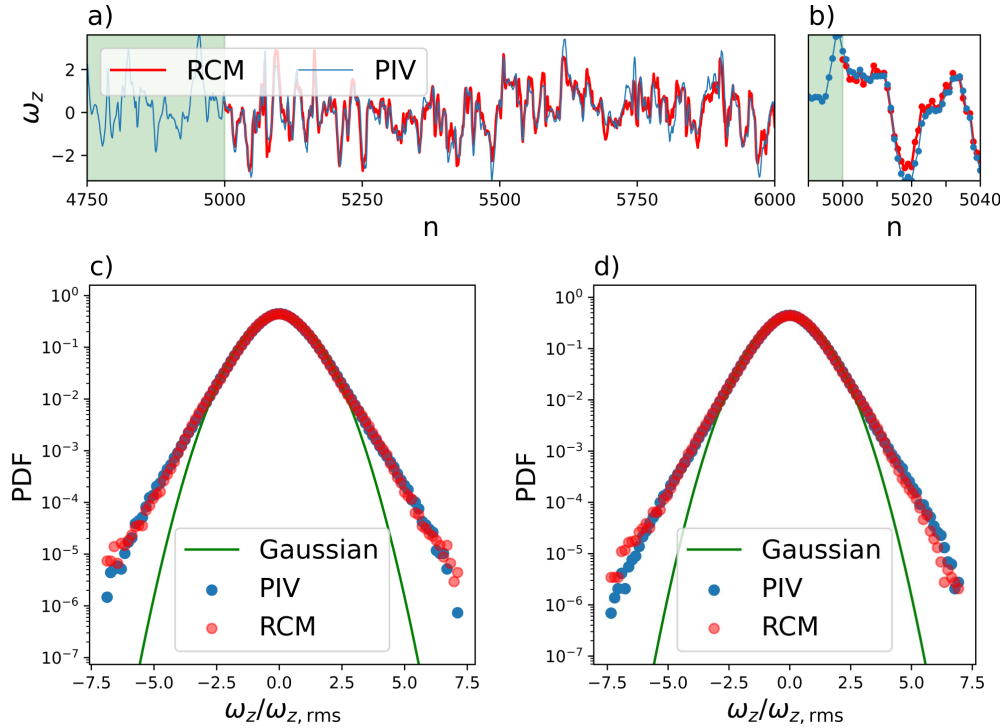


FIG. 9. Same as in figure 8 for  $Ra = 2.9 \times 10^5$  with  $\Delta t = 0.25t_{ff}$ .

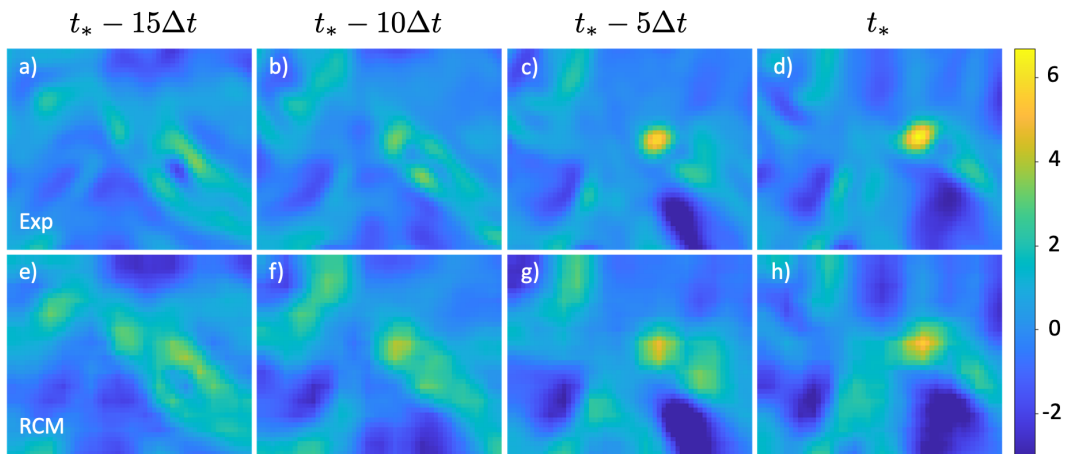


FIG. 10. Dynamical sequence of an extreme vorticity event (a–d) and its prediction by the reservoir computing model algorithm with the  $3 \times 3$  scenario (e–h). The extreme event of  $\omega_z$  is at time  $t = t_*$ . The time interval between two snapshots is  $\Delta t = 0.25t_{ff}$ . The Rayleigh number is  $Ra = 2.9 \times 10^5$ .

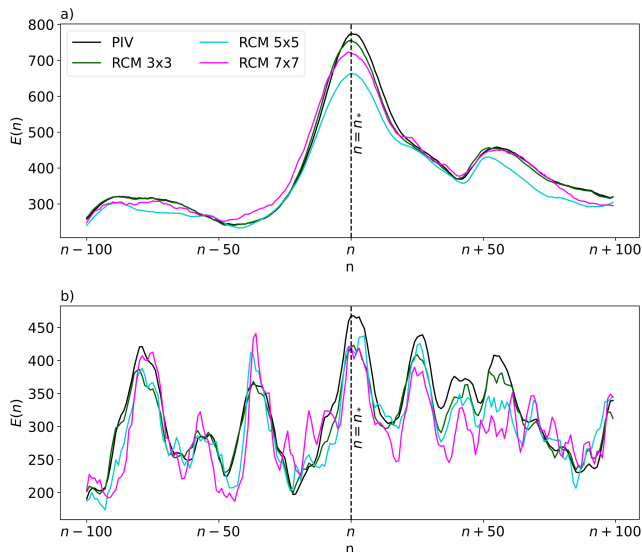


FIG. 11. Time series of the out-of-plane enstrophy  $E(n)$  for two Rayleigh numbers, (a)  $Ra = 1.7 \times 10^4$  and (b)  $Ra = 2.9 \times 10^5$  which is calculated by eq. (16). Both plots compare the measurement data with the reservoir computing predictions which have been obtained either by the  $3 \times 3$ , the  $5 \times 5$ , or the  $7 \times 7$  scenario as indicated in the legend of panel (a). Note that argument  $n$  stands for time  $t = n\Delta t$ .

nents of the turbulent convection flow were detectable in a horizontal section only and not fully resolved in the whole volume. Exceptions are high-resolution experiments which are practically almost as expensive in their postprocessing as fully resolved direct numerical simulations [46]. SPIV allows us to reconstruct 7 out of the 9 components of the velocity gradient tensor  $M_{ij}$  together with the out-of-plane vorticity component  $\omega_z$ . In many situations, such as field measurements, the time series

data are taken at sparsely distributed locations. These practical constraints suggest the application (recurrent) machine learning algorithms. They can process sequential data, make predictions on the dynamics, and thus add missing dynamical information on the turbulence fields. In the second part of this work, we had exactly such a proof-of-concept in mind when investigating the prediction capabilities of the applied reservoir computing model particularly those of extreme or high-amplitude vorticity events.

The studies can be extended in several directions. One direction would be a combination with temperature measurements close to the boundary layer, such that strong plume detachments can serve as precursors for extreme dissipation or vorticity events in the bulk of the convection layer. This idea has been developed in ref. [22] on the basis of fully resolved DNS. A further direction consists of the design of generative algorithms that produce time series of the missing 2 velocity derivative components complemented by the existing statistical symmetries in the flow at hand [47, 48]. In this way, machine-learning-assisted measurements of the kinetic energy and thermal dissipation rates would be possible without the usage of tomographic techniques. Studies in this direction are currently underway and will be reported elsewhere.

## ACKNOWLEDGMENTS

The authors would like to thank Alexander Thieme for the support with the experiments. The work of VV was partly supported by Priority Programme DFG-SPP 1881 on Turbulent Superstructures of the Deutsche Forschungsgemeinschaft (DFG). Her work is currently supported by the Marie Curie Fellowship of the European Union with project number

101024531. The work of RK is supported by project SCHU 1410/30-1 of the DFG. Training and prediction of the machine learning algorithm were carried out on up

to 8 CPUs of the compute cluster Makalu at Technische Universität Ilmenau.

- 
- [1] L. P. Kadanoff. Turbulent heat flow: Structures and scaling. *Phys. Today*, 54:34–39, 2001.
- [2] G. Ahlers, S. Grossmann, and D. Lohse. Heat transfer and large scale dynamics in turbulent Rayleigh-Bénard convection. *Rev. Mod. Phys.*, 81:503–537, 2009.
- [3] F. Chillà and J. Schumacher. New perspectives in turbulent Rayleigh-Bénard convection. *Eur. Phys. J. E*, 35:58, 2012.
- [4] M. K. Verma. *Physics of Buoyant Flows*. World Scientific, Singapore, 2018.
- [5] T. Hartlep, A. Tilgner, and F. H. Busse. Large scale structures in Rayleigh-Bénard convection at high Rayleigh numbers. *Phys. Rev. Lett.*, 91:064501, 2003.
- [6] A. Parodi, J. von Hardenberg, G. Passoni, A. Provenzale, and E. A. Spiegel. Clustering of plumes in turbulent convection. *Phys. Rev. Lett.*, 92:194503, 2004.
- [7] T. Hartlep, A. Tilgner, and F. H. Busse. Transition to turbulent convection in a fluid layer heated from below at moderate aspect ratio. *J. Fluid Mech.*, 554:309–322, 2005.
- [8] J. von Hardenberg, A. Parodi, G. Passoni, A. Provenzale, and E. A. Spiegel. Large-scale patterns in Rayleigh-Bénard convection. *Phys. Lett. A*, 372:2223–2229, 2008.
- [9] J. Bailon-Cuba, M. S. Emran, and J. Schumacher. Aspect ratio dependence of heat transfer and large-scale flow in turbulent convection. *J. Fluid Mech.*, 655:152–173, 2010.
- [10] M. S. Emran and J. Schumacher. Large-scale mean patterns in turbulent convection. *J. Fluid Mech.*, 776:96–108, 2015.
- [11] A. Pandey, J. D. Scheel, and J. Schumacher. Turbulent superstructures in Rayleigh-Bénard convection. *Nat. Commun.*, 9:2118, 2018.
- [12] R. J. A. M. Stevens, A. Blass, X. Zhu, R. Verzicco, and D. Lohse. Turbulent thermal superstructures in Rayleigh-Bénard convection. *Phys. Rev. Fluids*, 3:041501, 2018.
- [13] E. Fonda, A. Pandey, J. Schumacher, and K. R. Sreenivasan. Deep learning in turbulent convection networks. *PNAS*, 116:8667–8672, 2019.
- [14] G. Green, D. G. Vlaykov, J. P. Mellado, and M. Wilczek. Resolved energy budget of superstructures in Rayleigh-Bénard convection. *J. Fluid Mech.*, 887:A21, 2020.
- [15] D. Krug, D. Lohse, and R. J. A. M. Stevens. Coherence of temperature and velocity superstructures in turbulent Rayleigh-Bénard flow. *J. Fluid Mech.*, 887:A2, 2020.
- [16] P. Berghout, W. J. Baars, and D. Krug. The large-scale footprint in small-scale Rayleigh-Bénard turbulence. *J. Fluid Mech.*, 911:A62, 2021.
- [17] J. W. Deardorff and G. E. Willis. Investigation of turbulent thermal convection between horizontal plates. *J. Fluid Mech.*, 28:675–704, 1967.
- [18] D. E. Fitzjarrald. An experimental study of turbulent convection in air. *J. Fluid Mech.*, 73:693–719, 1976.
- [19] D. Schmeling, J. Bosbach, and C. Wagner. Simultaneous measurement of temperature and velocity fields in convective air flows. *Meas. Sci. Technol.*, 25:035302, 2014.
- [20] C. Kästner, C. Resagk, J. Westphalen, M. Junghähnel, C. Cierpka, and J. Schumacher. Assessment of horizontal velocity fields in square thermal convection cells with large aspect ratio. *Exp. Fluids*, 59:171, 2018.
- [21] C. Cierpka, C. Kästner, C. Resagk, and J. Schumacher. On the challenges for reliable measurements of convection in large aspect ratio Rayleigh-Bénard cells in air and sulfur-hexafluoride. *Exp. Thermal Fluid Sci.*, 109:109841, 2019.
- [22] V. Valori and J. Schumacher. Connecting boundary layer dynamics with extreme bulk dissipation events in Rayleigh-Bénard flow. *Europhys. Lett.*, 134:34004, 2021.
- [23] J. Schumacher, B. Eckhardt, and C. R. Doering. Extreme vorticity growth in Navier-Stokes turbulence. *Phys. Lett. A*, 374:861–865, 2010.
- [24] J. D. Scheel, M. S. Emran, and J. Schumacher. Resolving the fine-scale structure in turbulent Rayleigh-Bénard convection. *New J. Phys.*, 15:113063, 2013.
- [25] P. K. Yeung, X. M. Zhai, and K. R. Sreenivasan. Extreme events in computational turbulence. *PNAS*, 112:12633–12638, 2015.
- [26] D. Buaria, A. Pumir, and E. Bodenschatz. Self-attenuation of extreme events in navier-stokes turbulence. *Nat. Commun.*, 11:5852, 2020.
- [27] J. Schumacher and J. D. Scheel. Extreme dissipation event due to plume collision in a turbulent convection cell. *Phys. Rev. E*, 94:043104, 2016.
- [28] I. Goodfellow, Y. Bengio, and A. Courville. *Deep Learning*. MIT Press, Cambridge, MA, 2016.
- [29] H. Jaeger and H. Haas. Harnessing nonlinearity: Predicting chaotic systems and saving energy in wireless communication. *Science*, 304:78–80, 2004.
- [30] S. Pandey, J. Schumacher, and K. R. Sreenivasan. A perspective on machine learning in turbulent flows. *J. Turbul.*, 21:567–584, 2020.
- [31] Z. Lu, J. Pathak, B. R. Hunt, M. Girvan, R. Brockett, and E. Ott. Reservoir observers: Model-free inference of unmeasured variables in chaotic systems. *Chaos*, 27:041102, 2017.
- [32] P. A. Srinivasan, L. Guastoni, H. Azizpour, P. Schlatter, and R. Vinuesa. Predictions of turbulent shear flows using deep neural networks. *Phys. Rev. Fluids*, 4:054603, 2019.
- [33] P. R. Vlachas, J. Pathak, B. R. Hunt, T. P. Sapsis, Girvan M., E. Ott, and P. Koumoutsakos. Forecasting of spatiotemporal chaotic dynamics with recurrent neural networks: a comparative study of reservoir computing and backpropagation algorithms. *Neural Netw.*, 126:191–217, 2020.
- [34] S. Pandey and J. Schumacher. Reservoir computing model of two-dimensional turbulent convection. *Phys. Rev. Fluids*, 5:113506, 2020.
- [35] F. Heyder and J. Schumacher. Echo state network for two-dimensional moist Rayleigh-Bénard convection. *Phys. Rev. E*, 103:053107, 2021.

- [36] A. Asch, E. Brady, H. Gallardo, J. Hood, B. Chu, and M. Farazmand. Model-assisted deep learning of rare extreme events from partial observations. *arXiv:2111.04857*, 2021.
- [37] T. P. Sapsis. Statistics of extreme events in fluid flows and waves. *Annu. Rev. Fluid Mech.*, 53:85–111, 2021.
- [38] V. Valori. *Rayleigh-Bénard convection of a supercritical fluid*. Doctoral thesis, Delft University of Technology, 2018.
- [39] V. Valori, G. E. Elsinga, M. Rohde, J. Westerweel, and T. H. J. J. van der Hagen. Particle image velocimetry measurements of a thermally convective supercritical fluid. *Exp. Fluids*, 60:143, 2019.
- [40] R. J. Adrian and J. Westerweel. *Particle Image Velocimetry*. Cambridge University Press, Cambridge, UK, 2011.
- [41] M. Raffel, C. E. Willert, F. Scarano, C. J. Kähler, S. T. Wereley, and J. Kompenhans. *Particle Image Velocimetry: A Practical Guide*. Springer, Berlin, 2018.
- [42] E. W. Lemmon, M. L. Huber, and M. O. McLinden. NIST standard reference database 23: Reference fluid thermodynamic and transport properties-REFPROP, 2013.
- [43] J. Schumacher, J. D. Scheel, D. Krasnov, D. A. Donzis, V. Yakhot, and K. R. Sreenivasan. Small-scale universality in fluid turbulence. *PNAS*, 111:10961–10965, 2014.
- [44] J. Schumacher, A. Pandey, V. Yakhot, and K. R. Sreenivasan. Transition to turbulence scaling in Rayleigh-Bénard convection. *Phys. Rev. E*, 98:033210, 2018.
- [45] L. Lu and C. R. Doering. Limits on enstrophy growth for solutions of 3D Navier-Stokes equations. *Indiana Univ. Math. J.*, 57:2693–2727, 2008.
- [46] D. Schanz, S. Gesemann, and A. Schröder. Shake-The-Box: Lagrangian particle tracking at high image densities. *Exp. Fluids*, 57:70, 2016.
- [47] M. Mattheakis, P. Protopapas, D. Sondak, M. Di Giovanni, and E. Kaxiras. Physical symmetries embedded in neural networks. *arXiv:1904.08991*, 2019.
- [48] G. E. Karniadakis, I. G. Kevrekidis, Lu L., P. Perdikaris, S. Wang, and L. Yang. Physics-informed machine learning. *Nat. Rev. Phys.*, 3:422–440, 2021.